Strain field measurement on 3D surfaces: Application to petaloid base of PET bottles under pressure

Luc Chevalier, Yun Mei Luo, E. Monteiro, B. Plantamura

Editorial Manager(tm) for International Polymer Processing
Manuscript Draft

Manuscript Number: IP2327R1

Title: Strain Field Measurement on 3D surfaces: Application to Petaloid Base of PET Bottles under Pressure

Article Type: Review Article

Corresponding Author: Professor Luc Chevalier,

Corresponding Author's Institution: Université Paris-Est

First Author: Luc Chevalier, Professor

Order of Authors: Luc Chevalier, Professor; Yunmei Luo; Eric Monteiro; Bernard Plantamura

Manuscript Region of Origin: FRANCE

Abstract: Validation of stretched blown bottles of polyethylene terephthalate (PET) by using numerical simulation is an important industrial goal. This necessitates the identification of the PET material characteristics. Because the biaxial elongation of macromolecules induces great modifications of the mechanical properties of the material, it is difficult to manage an accurate simulation: properties are not well known in the base or neck region of the bottles.
The aim of the work presented here is to provide an identification tool for the orthotropic elastic properties in the 3D regions of PET bottles of soda waters. More specifically, we focus on the behavior of the petaloid bases when bottles are submitted to internal pressure like during burst or ESC (environmental stress cracking) tests.
A stereo correlation tool has been developed in order to build digital 3D surface; comparing the initial surface with the same surface when the bottle is under pressure, it is possible to evaluate the membrane strains at each point of the petaloid surface. Two bases, one with large valleys (VL) between the five feet and one with small valleys (VS) which highlight very different behavior at the ESC test, are compared with this tool.
Coupled with a finite element simulation managed on the same bases, these results allow the identification of the induced mechanical properties. The VL case presents specific characteristics that are discussed in the last section of the paper.

Answers for the editor and reviewers

Editor: The journal has changed the referencing format as of January, 2007 - please make sure your manuscript follows the new requirements.

The reference list has been checked and format modified as requirements.

Reviewer #1:
- This is a very interesting work in the sense that the results presented are new, well explained and contains a good literature review.

- Concerning the description of the stereo calculation method, I strongly suggest referring previous work(s) if possible or put some information given in the core of the article in the appendix. By doing this, it will be easier for the reader since the stereo correlation method is not necessary for understanding the explanation of the results presented.

All details on the stereo correlation calculation have been transported in an appendix. Figures and Equations have been renumbered

- It should be interesting to name small valley SV instead of VS, and the same for the large valley.

Done

- In Figure 4 description, the expression 'Strait Rectangle' should be replaced with 'Solid Rectangle'.

Done, figure 4 is now figure 15

Reviewer #2:
The work is of interest.
However beside an evident quality concerning mechanical approach paper is sometime unclear concerning correlation with microstructure. i.e., this latter is described as anisotropic whereas approach is isotropic.

Here, the text has been made clearer. It is well known that PET bottle highlights a clearly orthotropic elastic behaviour in the central part of the bottle and our results show that it is also the case in the petaloid base even if the difference between E1 and E2 is not so important in certain regions.

Author should be more clear in their introduction on to what extend their work is or is not related to microstructure.
If related to, than literature survey should be extended to other relevant works.
If not than a less "ambitious" introduction should be more relevant.

The reviewer's comment shows that our introduction insists too much on the microstructure and this point is not enough developed in our conclusions. In order to make both intro and discussion consistent we add a comment on the induced microstructure in the valley where low level of induced crystallisation appears in regard of the level in the middle part of the bottle.

Submitted to International Polymer Processing: November 2009
Revised manuscript submitted January 2010

Strain Field Measurement on 3D surfaces: Application to Petaloid Base of PET Bottles under Pressure

Luc Chevalier*, Yun Mei Luo, Eric Monteiro

Laboratoire MSME FRE3160 CNRS, Université Paris-Est

5 boulevard Descartes - Champs sur Marne

77454, MARNE LA VALLEE Cedex 2, FRANCE

Bernard Plantamura

SIDEL Group, Blowing & Coating division

Avenue de la Patrouille de France - Octeville sur mer

BP204, 76059 LE HAVRE Cedex, FRANCE

*corresponding author: luc.chevalier@univ-paris-est.fr

Abstract

Validation of stretched blown bottles of polyethylene terephthalate (PET) by using numerical simulation is an important industrial goal. This necessitates the identification of the PET material characteristics. Because the biaxial elongation of macromolecules induces great modifications of the mechanical properties of the material, it is difficult to manage an accurate simulation: properties are not well known in the base or neck region of the bottles.
The aim of the work presented here is to provide an identification tool for the orthotropic elastic properties in the 3D regions of PET bottles of carbonated soft drinks. More specifically, we focus on the behavior of the petaloid bases when bottles are submitted to internal pressure like during burst or ESC (environmental stress cracking) tests.
A stereo correlation tool has been developed in order to build digital 3D surface; comparing the initial surface with the same surface when the bottle is under pressure, it is possible to evaluate the membrane strains at each point of the petaloid surface. Two bases, one with large valleys (LV) between the five feet and one with small valleys (SV) which highlight very different behavior at the ESC test, are compared with this tool.
Coupled with a finite element simulation managed on the same bases, these results allow the identification of the induced mechanical properties. The LV case presents specific characteristics that are discussed in the last section of the paper.

Keywords

Stereo correlation, strain field measurement, polyethylene terephthalate bottles, petaloid base,

environmental stress cracking test, identification by coupled experimental-calculation

Strain Field Measurement on 3D surfaces: Application to Petaloid Base of PET Bottles under Pressure

1. Introduction: modeling the stretch blow molding process

The polyethylene terephthalate (better known as PET) is a thermoplastic (saturated polyester family) that can be found either in amorphous or semi-crystalline state. In the range of temperature between T_g and T_m, the chains of the amorphous phase are able to change their conformation and the thermal energy is low enough not to destroy the crystals that could be created. If enough time is given, the macromolecules are able to get closer and to organize in crystalline zones. An other way for PET to crystallize is the strain induced one: under a fast elongation (stretching) macromolecules may align, chains can get closer and this induces a change from cis- to trans-conformation (Shen et al., 1991, Spiby et al., 1992, Lapersonne et al., 1992) which induces a partial crystallization. The chains are organized in a first time in micellar structures (Haudin and Monasse, 1996) and then in crystalline lamellae. The limited dimensions of these structures (0.1 to 0.9 nm) keep a good transparency of the stretched and crystallized PET as it can be observed for PET bottles.

The strain induced crystallization phenomenon has been observed for very various strain states: simple shear (Titomanlio et al., 1997, Popple et al., 2000), uni-axial tension (Salem, 1992, Lapersonne et al., 1992, Marco, 2003), plane, biaxial or sequenced tension tests (Cakmak et al., 1986, Chang et al., 1993, Marco et al., 2002) and for different kind of solicitations: constant force, constant speed or constant strain rate tension tests (Le Bourvellec et al., 1986, Le Bourvellec and Beautemps, 1990, Vigny et al., 1997, Salem, 1998). Molecular mechanisms seem to be the same in all these studies but the induced microstructure shows differences on crystallinity ratio, amorphous and crystalline chains orientation and crystals size. In a recent study, (Hanley et al. 2006) collected SAXS data with a 100 μm square X-ray

beam in the petaloid bases of PET bottles to establish the molecular morphology as a function of position across the base topology. An amorphous region was identified in the base center (i.e., close to the injection point of the preform) with biaxially orientated, semicrystalline regions in the feet and valleys of the bottle bases. For bottles that had failed to ESC test, the transition between these two regions displayed uniaxial orientation that would lead to reduced mechanical strength in the circumferential direction. More recently, microstructure evolution followed by WAXS and SAXS on blown parts clearly show that the microstructure can differ along the bottle and from processing conditions to another. From these measures, Picard and Billon, 2007, suggested that the strain hardening effect was related to the evolution of a mesophase that exhibits a higher density than the amorphous phase.

Nevertheless, the morphology and, consequently, the final mechanical properties of stretch blow-molded PET bottles are largely dependent of the strain history during the process. In Chevalier et al 1999, for example, it has been shown that the Young modulus of the amorphous preform could be multiplied by more than 2 in the longitudinal direction and by more than 3 in the circumferential direction of the cylindrical region of a blown bottle: consequently, isotropic elasticity of the amorphous PET of the preform becomes orthotropic in the blown bottle.

The knowledge of these properties is necessary to assess, by a numerical simulation, the ability of bottles to resist to internal pressure or palletizing. In particular, in the petaloid bases of PET bottle, the strain history is very different from one region to another and the stretch blow molding process induces a heterogeneous distribution of Young modulus and yield stress. The manner how PET has been stretched has an important influence on the resistance and large variations related to the base design are observed on the time before stress-cracking during an ESC test.

Consequently, it is difficult to manage a finite element simulation of the base behavior of a blown bottle under pressure until the mechanical properties are not known accurately. Previous study presented in Chevalier et al. 1999 gives accurate values of the orthotropic elastic behavior in the regular region of a blown bottle from classical measures managed on specimen cut out from blown bottles. In order to collect more data in 3D blown shapes where it is difficult to cut tension specimen, we focus on a more complex part of the bottle: the petaloid base. PET is not as stretched in that region and mechanical properties are lower than in the body region of the bottle.

We present an identification procedure to define the modulus distribution in the petaloid base. The procedure involves an experimental aspect where a stereo correlation technique is developed to build the strain field on the 3D surface of the petaloid base. The digital image correlation has been developed at the beginning of 80's: Peters et al. 1982, Peters et al. 1983, Sutton et al. 1983, for example, applied this technique in the rigid bodies mechanics, particularly for 2D problems (He et al. 1984, Sutton et al. 1986, Bruck et al. 1989). This method is now widely used to measure, without disturbing, the mechanical response of a heterogeneous material under plane strain or plane stress (Reynolds et al. 1999, Yan et al. 2006).

Later, the digital image correlation was extended to 3D bodies (Luo et al. 1994, Helm et al. 1996, Garcia et al. 1999) by using a stereovision system with two cameras to recognize 3D objects by their boundary shape. Garcia et al. 2002, have used this technique to measure an initial 3D surface and the displacement field of the same surface under loading. The triangulation principle is used for example in Garcia et al. 2002, Mistou et al. 2003 to determine the 3D coordinate from the intersection of two optical lines coming from two points in correspondence. The correspondence problem is to find, in each image, the representation of the same point.

One difficulty of the stereovision is to establish the correspondence between the pair of digital images. The stereo correlation technique has been proposed and applied by Hamid since 1996 for example. Hild et al. 1999, developed in the Matlab environment, a digital image correlation software named Correli which allows comparing two digital images of a surface covered with random spots. Using the fast Fourier transformation, the software put in relation the corresponding points of both images. The difference (δx, δy) between the same point in the two images can be used whether to build the plane displacement field in the 2D case or to build the 3rd coordinate in the case of a 3D surface.

Recent studies (Réthoré et al. 2007, Réthoré et al. 2009) use an extended technique for images correlation which, coupled with the X-FEM can reach discontinuities in the displacement field independently of the mesh choice. Other extensions of the digital correlation technique are proposed by Roux et al. 2008: from digital images obtained by X Ray microtomography, the inside of an object may be reached and the 3D displacement field is built.

Here, we used the Correli software extended to large strain for polymer studies. This software has already been presented in Chevalier et al. 2001 or Chevalier et al. 2002 and since the distance between cameras is small (200 mm) compared with the distance between the cameras and the objects (about 2 m), the geometrical problem of the correspondence is reduced to a simple linear expression between (δx, δy) and the 3rd coordinate z. We apply the technique to the case of petaloid bases.

These experimental results are compared with finite element simulations managed on the same geometry. The comparison leads to the distribution of the elastic properties over this surface. Developments are illustrated on two different designs of petaloid bases which exhibit very different performances during the ESC test. Both bases are named SV (small valley) and LV (large valley) in reference of the region between two feet.

In the “experimental” section, the ESC test is described and differences between the results of the petaloid bases LV and SV are highlighted. The 3D surface measurement apparatus is also presented, and the accuracy of the method is shown on two specific geometries: a cylinder with given radius and a parallelepiped bloc with sharp edges.

In the “modeling” section, the theoretic aspects of the 3D strain field measure are recalled and applied to the measurement of the strain field in the quasi cylindrical part of a soda PET bottle under pressure. In order to compare results a finite element modeling of a PET bottle under pressure is also presented. An elastic orthotropic model is chosen to represent the PET behavior.

In the “result and discussion” section, the 3D strain field measurement is applied to both SV and LV petaloid bases under pressure. The results are compared to the finite element simulation and a procedure is managed to carry out the identification of the modulus distribution. Correlation between this distribution and the resistance to ESC test is discussed.

2. Experimental measurements

Sidel developed two bottle petaloid bases which exhibit radical different behavior, especially during the ESC test. The first base (LV) is designed with large valley between each one of the five feet, and feet sides are nearly parallel. On the other hand, the second base (SV) has a small valley between two feet and the feet sides are less straight than on the LV base (see Fig.1).

In this section we first present the results of the ESC test on both bases and, next, we present the stereo correlation measures that have been made to provide the principal strain fields on the petaloid base surface.

2.1 Environmental Stress Cracking (ESC) test

Environmental Stress Cracking (ESC) is one of the most common causes of unexpected brittle failure of thermoplastic polymers. ESC and polymer resistance to ESC have been studied for

several decades. Xiangyang, 2005, shows that the exposure of polymers to liquid chemicals tends to accelerate the crazing process, initiating crazes at stresses that are much lower than the stress causing crazing in air. The action of either a tensile stress or a corrosive liquid alone would not be enough to cause failure, but in ESC the initiation and growth of a crack is caused by the combined action of the stress and a corrosive environmental liquid.

Both SV and LV petaloid base have been submitted to the ESC test. The bottle is pressurized to 5.3 bar internal pressure, and the base is drowned in a 0.2% caustic soda solution. The goal is that the bottle resists more than 10 minutes before bottle bursting or leaking.

Numerous parameters influence this resistance (the chosen polyester, the injection conditions of the preform, the design of the preform and the design of the base, the stretch blow moulding conditions…) and the time before cracking presents a large dispersion.

On table 1, one can see that the standard variation is almost the same for the two designs of the petaloid base, but the mean value is clearly lower for small valley, most of the tested bottles cannot reach the 10 min and the design is not validated. Building the probability density function for the "time before cracking" variable, one can define the confidence region for 95% of the tests for each design (figure 2). In the SV case, the confidence region is [1.2, 47 min]. In the case of the LV base, the confidence region is [28.5, 74.1 min]: very few bottles will be rejected during the test for this design.

One goal of the following sections is to explain the origin of such a difference between the two bases. Analysis of the petaloid base deformation under pressure will help to understand the difference of performance under the ESC test.

2.2 Surface construction by stereo correlation

In this section we present the construction of a 3D surface from two digital images, we discuss caution that have to be taken and we quantify the accuracy of the method by testing two significant cases: a given cylinder and a parallelepiped bloc. The stereo correlation

technique is based on the determination of the apparent displacement between two digital images of the same object taken by two cameras (Fig.3). The digital image correlation software named Correli^{GD} (Chevalier et al., 2001) has been adapted to transform displacements U and V of a node of the grid into the depth z of a point M of the 3D object. Details on this adaptation are given in the appendix.

Figure 4 shows a cylinder and a parallelepiped bloc prepared with random spots. The region of interest is highlighted on the picture and represented in perspective and along the Y direction. Qualitatively, the 90° angle of the bloc and the cylindrical shape of the cylinder are well represented by the stereo correlation technique. The cylinder diameter is equal to 44.7 mm, the value of parameter a is fixed to 100 mm and the d value is around 2000 mm so that the angle between the cameras does not exceed 2α where α=0.05 rd. If α is greater, the apparent displacement necessitates either a more complex geometrical development, or a large mask size (typically greater than the maximum apparent displacement between the two pictures). In these conditions, the stereo correlation technique applied to the cylinder allows the determination of the radius of the best cylinder that fits the measured points by a least square method. This radius varies with the value of d given and the reel cylinder radius is obtained for d=1850 mm. This is the value that takes into account the focal of the cameras and the position of the reference point of the 3D object. The reference point is the one for which apparent displacement δV=0 and that defines the z origin.

In the case of the bloc, one is interested by the accurate representation of a sharp angle of 90°. The sharpness is represented by the "radius" at the junction of the two plane sides. To evaluate the capacity of the technique to determine the 90° angle between the 2 sides, we use the least square method once again, to determine the equation of the best plane. Product between the coefficients of the two equations, that is supposed to be equal to -1, gives the angle which is compared to 90°.

First, when the mask size is M=128 pixel, it appears that the best results are obtained when the shift S is small (about 8 to 16 pixel) and the T smoothing parameter is small (T=1 or 2). In that condition the error on the angle value is less than 1° and the "radius" between the tow plane sides is less than 3 mm on a side that measures 100 mm. This last precision on the "sharpness" of an angle is directly related to the shift factor and cannot be reduced under 1 or 2S. The smoothing parameter T also obviously influences the "sharpness" of the angle and the smallest value gives the best results. On the other hand a smoothing operation is necessary to evaluate accurate strain values and the best compromise is obtained for T=1 or 2 when S = 8 or 16.

These parameters appear to be also the best choice for the cylinder dimension precision. In that case, the diameter is obtained with a sub pixel precision. It is worth noting that even in case of a slight imprecision on the dimensions due to a wrong evaluation of the distance d, the error is similar in the initial surface and in the deformed surface after application of a load on the object: the strain value, which is a ratio between initial and final dimensions, is not affected. The technique has been applied to a 3D petaloid base visualization: first when the PET bottle is empty and free of load, second when the same bottle is under a 5 bar internal pressure. Figure 5 visualizes the initial surface and the displacement field from the initial and deformed surface, for the two different bases SV and LV.

The left shape is the SV shape where one can see the effect of the internal pressure: injection point and feet move quasi homogeneously in the Z direction which is representative of a global expansion of the bottle due to the pressure. The right shape is the LV shape and one can see that the behavior under pressure is totally different: feet move in the Z direction while the injection point remains still. The base design leads to a bending phenomenon where each foot rotates around the injection point. Both bases react differently to the load and it is not so

surprising that performances to ESC test are different. We will confirm this in the following with the strain evolution versus pressure.

2.3 Thickness measurements

During the stretch blow molding process, the rod pushes the base of the preform near the bottom of the mould and the initial thickness does not decrease very much in that region near the injection point. Elsewhere, the material of the preform is biaxially stretched and the initial thickness decreases from about 3 mm to about 0.3 mm.

The thickness of the final blown bottle varies a lot near the injection point and one needs to know accurately the distribution to explain the petaloid base behavior when bottles are under pressure. Figure 6 shows the two bases SV and LV that have been cut and measured. The chart shows the thickness versus the distance from the longitudinal axis of the bottle (Radius). One can see that the distribution in the valley and the distribution on the feet are quasi identical. Considering the small dispersion between the thickness evolution in the feet side and the valley side, a unique interpolating function e(r) is chosen to specify the thickness versus the radius from the bottle longitudinal axis.

$$e(r) = (e_M - e_\infty)\exp\left(-\left(\frac{r - r_0}{L}\right)^2\right) + e_\infty \qquad (1)$$

e_∞ is the uniform thickness far from the injection point, e_M is the maximum thickness, r_0 is the radius where the thickness is maximum and L is a characteristic decreasing length of the thickness evolution. Values of these parameters are given in Table 2. They are slightly different for SV or LV bases. These functions will be implemented in Nastran to manage the numerical simulation of the bottles submit to internal pressure.

3. Theoretical basics of the identification method

To provide an accurate identification of the material properties, we choose to couple experimental results on the 3D surface of the petaloid base with the results of numerical

simulation managed using large displacements basics on the same geometry: the petaloid base. First we present the strain field components calculation done from the stereo correlation technique described in the first section. Then, we present the finite element model and boundary conditions imposed to simulate the same deformation step and the method and assumption made to identify the heterogeneous and anisotropic elastic behavior of the final bottle.

3.1 Strain field calculation

The stereocorrelation technique allows the determination of the z coordinate for each point of the reference picture supposed to be in the plane $\left(\vec{x}, \vec{y}\right)$. The 3D surface is then described as a function z = f(x,y) and one can compute the displacement components U, V and W by comparing the initial surface with the deformed surface (when the bottle is under pressure). U, V and W are also functions of coordinates x and y so the derivatives of the strain tensor in the reference base $\left(\vec{x}, \vec{y}, \vec{z}\right)$ are reduced to:

$$\varepsilon_{XX} = \frac{\partial U}{\partial x}; \varepsilon_{YY} = \frac{\partial V}{\partial y}; \varepsilon_{ZZ} = 0; \varepsilon_{XY} = \frac{1}{2}\left(\frac{\partial U}{\partial y} + \frac{\partial V}{\partial x}\right); \varepsilon_{XZ} = \frac{1}{2}\frac{\partial W}{\partial x}; \varepsilon_{YZ} = \frac{1}{2}\frac{\partial W}{\partial y} \qquad (2)$$

One can deduce the membrane strain (i.e., the strain in the surface) by applying the projection tensor Π in the tangent plane to the 3D surface at the considered point M. First, it is necessary to build the local base $\left(M, \vec{n}, \vec{t}, \vec{s}\right)$.

3.1.1 Surface construction, projection operator

Figure 7 gives a representation of the surface and the local base near the point M(x,y,z)= f(x,y). $\vec{t_x}$ and $\vec{t_y}$ are the two local vectors included in the tangent plane and that project in $\vec{X}$ and $\vec{Y}$. From these two vectors, one can calculate the normal vector $\vec{n}$.

$$\vec{t_x} = \frac{\partial \overrightarrow{OM}}{\partial s_x} = \cos\theta_x \vec{X} - \sin\theta_x \vec{Z} \qquad (3)$$

$$\vec{t}_y = \frac{\partial \overrightarrow{OM}}{\partial s_y} = \cos\theta_y \vec{Y} + \sin\theta_y \vec{Z} \qquad (4)$$

$$\vec{n} = \frac{\vec{t}_x \wedge \vec{t}_y}{\left\| \vec{t}_x \wedge \vec{t}_y \right\|} = \frac{1}{\cos^2\theta_x + \sin^2\theta_x \cos^2\theta_y} \begin{bmatrix} \sin\theta_x \cos\theta_y \\ -\cos\theta_x \sin\theta_y \\ \cos\theta_x \cos\theta_y \end{bmatrix} \qquad (5)$$

Because the base obtained is generally not orthogonal, one can complete the base formed by $\vec{t}_x = \vec{t}$ and $\vec{n}$ to obtained a second vector of the tangent plane $\vec{s}$:

$$\vec{s} = \vec{n} \wedge \vec{t} = \frac{1}{\cos^2\theta_x + \sin^2\theta_x \cos^2\theta_y} \begin{bmatrix} \cos\theta_x \sin\theta_x \sin\theta_y \\ \cos\theta_y \\ \cos^2\theta_x \sin\theta_y \end{bmatrix} \qquad (6)$$

Membranes strains $\underline{\underline{\varepsilon}}_{(\vec{t},\vec{s})}$ are obtained by the projection of the 3D strain tensor previously evaluated in the $(\vec{x}, \vec{y}, \vec{z})$ base:

$$\underline{\underline{\varepsilon}}_{(\vec{t},\vec{s})} = \Pi \; \underline{\underline{\varepsilon}}_{(\vec{X},\vec{Y},\vec{Z})} \; \Pi^T \qquad (7)$$

Where:

$$\Pi = \begin{pmatrix} t_x & t_y & t_z \\ s_x & s_y & s_z \end{pmatrix} \qquad (8)$$

This operation provides the components $\varepsilon_{tt}, \varepsilon_{ss}, \varepsilon_{st}$ of the $\underline{\underline{\varepsilon}}_{(\vec{t},\vec{s})}$ local strain tensor from where it is easy to compute the principal membranes strains by relations:

$$\varepsilon_1 = \frac{\varepsilon_{tt} + \varepsilon_{ss} + \sqrt{(\varepsilon_{tt} - \varepsilon_{ss})^2 + 4\varepsilon_{st}^2}}{2} \quad \text{and} \quad \varepsilon_2 = \frac{\varepsilon_{tt} + \varepsilon_{ss} - \sqrt{(\varepsilon_{tt} - \varepsilon_{ss})^2 + 4\varepsilon_{st}^2}}{2} \qquad (9)$$

The principal strain directions $(\vec{k}_1, \vec{k}_2)$ are included in the tangent plane defined by $(\vec{t}, \vec{s})$. The angle θ between $\vec{k}_1$ and $\vec{t}$ is obtained by relations:

$$\sin(-2\theta) = \frac{2\varepsilon_{st}}{\sqrt{(\varepsilon_{tt} - \varepsilon_{ss})^2 + 4\varepsilon_{st}^2}} \quad \text{and} \quad \cos(-2\theta) = \frac{\varepsilon_{tt} - \varepsilon_{ss}}{\sqrt{(\varepsilon_{tt} - \varepsilon_{ss})^2 + 4\varepsilon_{st}^2}} \qquad (10)$$

3.1.2 Application to the petaloid base of PET bottles

The stereocorrelation method described in the previous sections has been applied to the SV and LV petaloid bases of PET bottles under 5 bar of internal pressure.

Figure 8a shows a picture of a petaloid base with the grid of the studied zone and specially the circle which delimitates the zone of interest: outside this circle the values of the apparent displacement V becomes important in regard of the size M of the mask, and the convergence of the correlation technique may not be guaranty for all nodes of the grid. Consequently, we set to zero the values of the principal strains for all nodes outside this circle.

Figures 8b and 8c show the principal strain distribution on the zone of interest of the SV petaloid base and below the principal direction associated. One can see that ε_1 is positive everywhere. Starting from about 0.6% near the injection point, the strain increases up to nearly 1% on the feet but quickly reaches 1.5% in the valleys that are more stretched than feet. The principal direction associated with this elongation is nearly radial everywhere. Obviously not near the injection point because the strain is equibiaxial but in the valley and on top of the feet the 1rst principal direction is radial. On the edges of the feet principal direction turns and is oriented in the greatest slope direction. On these edges, the direction associated to ε_2 is quasi radial.

ε_2 is positive near the injection point and negative elsewhere, especially in the valley where the surface is stretched in direction 1 (nearly radial) so that length decreases in direction 2. Figures 8d and 8e provide the same information for the LV petaloid base. One can see that strain distribution ε_1 is identical in the valley but lower on feet than for the SV base. Considering ε_2, one can see that strain is higher on the feet than for the SV base. It is near the injection point that the differences are more important. Principal direction are quasi identical to the SV case excepted for the feet edges where principal directions are more or less ±45° from the greatest slope direction.

On Fig. 9, we focus at the injection point where the strain state is quasi biaxial ($\varepsilon_{xx} \sim \varepsilon_{yy}$ and $\varepsilon_{xy} \sim 0$ not plotted) even if some dispersion occurs from one test to another. One can see that the behavior of the SV base is quasi linear from 0 to 5 bar of internal pressure. When pressure increases more than 5 bar permanent strain occurs; the behavior is no more elastic. For LV base the behavior is clearly not linear and this, even for very low level of pressure: permanent strains cannot be the explanation, we have here a geometrical effect. The geometry of the feet leads to a first bending effect where feet come together towards the axis of the bottle. This leads to a compression on the outside skin of the bottle surface. Then, when pressure increases, the inflation of the bottle has an opposite effect and strain becomes positive.

One can also notice that for the same pressure (5 bar), the strain level is about six times lower for LV than for SV which is a important difference of behavior that may be put in relation with the better resistance of LV bases in the ESC test.

3.2 Numerical – Experimental comparison

In this section, we suppose that stress distribution is not affected by the behavior of the material. This is obviously true in a regular zone like the cylindrical part of a soda bottle where circumferential and longitudinal stresses are related to the internal pressure P by the relations σ_θ =PR/e and σ_z=PR/2e where R is the cylinder radius and e the thickness. This result only comes from the equilibrium equation and is true either for isotropic or anisotropic materials. It could be different in region where the bottle geometry is more 3D but, since the stress field is directly related to the internal pressure, we will obtain a good evaluation of the stress field (but certainly a bad representation of the strain field) by an isotropic elasticity calculation (with E=1200 MPa and υ=0.38).

3.2.1 Stress field evaluation

The numerical simulation is managed using Patran-Nastran software. The CAD models of the bottle and petaloid bases provided by Sidel have been meshed with linear shell elements. It

worth noting that finite element simulation have been managed on the finite element model of the entire bottle and that it gives the same stress distribution in the base region apart of some edge effects where boundary conditions are applied. In the following we reduce our study by considering the finite element model of the base only.

About 24000 nodes have been used to make sure of the accuracy of the numerical solution (Fig. 10a). The boundary conditions applied on the top circle: $u_\theta = u_z = 0$; only the radial expansion u_r is free for the nodes of this line. Rotations degrees of freedom have also let free; we tested the difference between rotations free or locked and this does not make much difference in the stress field. Figure 10b shows the implementation of the thickness evolution e(r) that has been measured on the bottle base as shown on Fig.6.

The principal stresses σ_1 (the major one to put in relation with ε_1) and σ_2 are represented on Fig.11a and 11b; both are in tension on the outside skin of the surface and since the thickness is small, one can suppose the same stress field exists on the inside skin of the bottle. One can compare the principal direction (Fig.11c) of the stress distribution with the principal direction of the measured strains (Fig.8): this direction is radial in the valley and almost every where on the feet. We can notice some differences on the edges of the feet and also along the symmetry axis of the feet where the principal direction becomes circumferential during a small region. This may generate difficulties when identifying the modulus.

Because the thickness increases near the injection point, we focus on that node on Fig.12. The evolutions of the inside and outside stresses are plotted and one can see the strain state is purely biaxial at this point. For the SV base (Fig.12a) one can notice the linearity of the behavior but also the difference between the tension stress on the outside skin which reaches higher values than on the inside skin. This proves the existence of bending stress superposed to the mean stress that is tension (about 16 MPa for 5 bar). The bending effect (about ±5 MPa) is small in regard of the tension for SV.

On Fig.12b, one can see that the behavior of the LV base is non linear (due only to geometry) and clearly different from SV.

Two steps can be observed: from 0 to 1.5 bar, we have a bending effect where tension is on the inside skin of the bottle and compression on the outside; from 1.5 bar and higher pressure, the bending changes side and the compression is located on the inside skin and tension on the outside as in the SV case. One can also notice that the bending effect (about ±3 MPa) is small in regard of the tension effect which reaches 14 MPa for 5 bar.

3.2.2 Identification of an orthotropic behavior

On one hand, we consider the stereo correlation tool presented in section 2 to determine, at each point of the petaloid base, both principal strains ε_1 and ε_2 related to principal directions principals $\overrightarrow{k_1}$ and $\overrightarrow{k_2}$. On the other hand, using an isotropic and homogeneous elastic finite element calculation, we determined both principal stresses σ_1 and σ_2 by using Patran-Nastran with the non linear geometry option. Assuming that the principal directions are identical in both cases, and that they are equal to the orthotropic directions (This last assumption seems to be very hazardous but in the case of stretch blow molding one can justify it easily. During the process, the rod provides longitudinal elongation of the macromolecular structure and then internal pressure blows the elongated preform and generates a radial expansion of macromolecules. The stresses generated during the ESC test reproduces the ultimate step of the blow molding process and it is a good approximation to take principal stress direction as the orthotropic direction in that case. Obviously, it would be very hazardous if we were simulating a top load test for example) one can identify the orthotropic elastic properties: four parameters (E_1, E_2, υ_{12} and υ_{21}) are to be found from the following system.

$$\begin{aligned} \varepsilon_1 &= \frac{\sigma_1}{E_1} - \frac{\upsilon_{21}\sigma_2}{E_2} \\ \varepsilon_2 &= \frac{\sigma_2}{E_2} - \frac{\upsilon_{12}\sigma_1}{E_1} \end{aligned} \qquad \text{with: } \frac{\upsilon_{12}}{E_1} = \frac{\upsilon_{21}}{E_2} \qquad (11)$$

The balance between relations and unknown variables is not satisfied and more, the relation that imposes the symmetry of the elasticity tensor imposes larges differences between υ_{12} and υ_{21}. As shown in Chevalier et al., 1999 typical Young modulus measured for injected amorphous PET is about E_0 = 1200 MPa with a 0.38 Poisson's ratio. Since the macromolecules are stretched during the forming process, the properties may increase much to reach about $E_L \sim 2E_0$ MPa in the longitudinal direction and $E_T = 3E_0$ in the circumferential one. This 2/3 ratio between modulus must be the same between the Poisson's ratios which may lead to values over 0.5 if no caution are taken in the identification process.

On the other hand, Poisson's ratio is related to the volume variation under load: most flexible polymers do not highlight any volume variation when stretched (rubbers for example); their Poisson's ratio is 0.499. For LDPE (υ=0.48) or PP (υ=0.43), which are quite flexible, the Poisson's ratio remain near 0.5. At the opposite, rigid polymers as PS, PMMA, PC or PET have lower Poisson's ratio (about 0.37-0.38). Consequently, the increase of the Young modulus should lead to a decreasing of the value of the Poisson's ratio. If we assume that the modulus E_1 is greater than E_2, then the υ_{12} will be greater than υ_{21}. We set υ_{12} to υ_0 in our identification procedure and consequently none of Poisson ratios will exceed 0.5.

$$\upsilon_{12} = \upsilon_0 \rightarrow \begin{cases} \varepsilon_1 = \dfrac{\sigma_1}{E_1} - \dfrac{\upsilon_0 \sigma_2}{E_1} \\ \varepsilon_2 = \dfrac{\sigma_2}{E_2} - \dfrac{\upsilon_0 \sigma_1}{E_1} \end{cases} \qquad (12)$$

From these two relations, one can easily compute E_1 and E_2:

$$E_1 = \frac{\sigma_1 - \upsilon_0 \sigma_2}{\varepsilon_1} \quad \text{and} \quad E_2 = \frac{\sigma_2 \left(\sigma_1 - \upsilon_0 \sigma_2 \right)}{\varepsilon_2 \sigma_1 - \upsilon_0 \left(\varepsilon_1 \sigma_1 + \varepsilon_2 \sigma_2 \right)} \qquad (13)$$

For example, at the injection point where the strain and stress fields are purely biaxial ($\varepsilon_1 = \varepsilon_2$ = 0.5% and $\sigma_1 = \sigma_2$ = 20 MPa), one can calculate the Young modulus E_1 (= E_2) to 2400 MPa, which is the characteristic value of the amorphous modulus for this injected PET.

4. Results and discussion

4.1 Elastic properties distribution in petaloïd base

The SV petaloid base

Considering the linear behavior of the SV petaloid base, we can apply the procedure described in the previous section and compute the maps of the modulus E_1 and E_2 as shown on Fig.12. For each node M_i of the grid include in the circle of the zone of interest, values of ε_1 and ε_2 are stored as well as the coordinates x_i, y_i, z_i. We find the element of the finite elements mesh which includes this node and store the stress values of σ_1 and σ_2 on the outside skin of the element. σ_1/ε_1 and σ_2/ε_2 ratios are formed in order to evaluate the most rigid direction and to affect the highest Poisson's ratio. Modulus E_1 and E_2 are then computed and the assumption made on the highest one is verified.

One can see on Fig.13 that the region near the injection point is not re-enforced and both modulus E_1 and E_2 are equal to the amorphous PET value. The modulus E_1 increases when we follow the radial direction towards the feet but not in the valley where the modulus remains low. One can also notice that the distribution of E_2 is not similar to the distribution of E_1, especially on the feet, which means that the material had become anisotropic during the process. The material is certainly more stretched during the process in the radial direction in regard of the circumferential direction to form the feet (which is the opposite of what happens in the cylindrical region of the bottle where circumferential elongation is higher than the longitudinal that becomes radial in the base) and the induced modulus are then different. The induced anisotropy is not as important than in the central part of the bottle but the feet are clearly anisotropic.

The LV petaloid base

In the case of the LV petaloid base, the results are not satisfactory because of the geometrical non linear behavior of the base. In particular, one can see that even if the stress (Fig.12b) shows an evolution similar to the strain; the outside strain is first negative and then positive while the outside stress is always positive. In this region where $\varepsilon_1 = \varepsilon_2 = \varepsilon$ and $\sigma_1 = \sigma_2 = \sigma$ and the two relations of Eq. 15 leads to a unique relation:

$$\varepsilon = \frac{(1-\upsilon_0)\sigma}{E} \qquad (14)$$

Stress and strain at the injection point must be the same sign and follow the same evolution until the material is purely elastic.

Consequently, when we compare strains and stresses for low level of pressure: negative strains and positives stresses lead to identification of negative Young modulus which is not acceptable. For the same reasons, if we compare the important stresses and the very low strains obtained for higher values of pressure, the identification leads to very high level of modulus which is not compatible with the microstructure observed on the LV base.

Figure 14 compares the morphology of a SV base and a LV base. Both bases have been heated at 120°C during more than half an hour and all amorphous zones have crystallized. One can see that a quasi circular white zone of 20 mm radius has completely crystallized for both bases, that proves that the PET was initially amorphous in that zone. This is confirmed by the thickness value in that zone that are still of 1.5 to 2 mm which shows that PET has not been stretched much and has no reason to increase its Young modulus in that region. The area of this amorphous region can be compared with the zone where the Young modulus E_1 and E_2 are quasi equal and equal to E_0: consequently, the origin of the modulus increasing has to be found in the change of morphology.

4.2 Correlation between ESC and strain field

Despite the difficulties to realise the identification in the LV petaloid case, it seems that the increase of elastic properties are similar to the SV case. The same shapes of the white zones in the pictures of Fig. 14 seem to prove that the PET has been stretched almost identically for both bottles. This should be confirmed with modulus measures directly managed on specimen cut out from the bottle base in region where the 3D surface is developable. If assumed that the no difference comes from the elastic behaviour, the geometry of the base is only responsible for the significant difference of performance to the ESC test.

First, one can see on Fig. 15 that the region where cracks appears (feet side at about 12 mm from the injection point) the first principal strain is positive (elongation in the radial direction) and the second principal strain decreases to zero and becomes negative (small contraction in the circumferential direction). It is well known that materials that obey to the von Mises criteria have a better resistance in biaxial stretching than in plane strain or uniaxial elongation strain which is the case in this region. It is not surprising then that cracks appear here, and because of the orientation of the associated principal direction (radial) the cracks initiates in the circumferential direction and then propagates straight cutting the other feet.

Second, the bending effect of the LV base, leads to smaller strains for 5 bar pressure than in the SV case. At equal strength, if the higher principal strain is 5 to 6 times lower for this base, stresses should be the same and that explain why the LV petaloid base is more resistant than the SV one to stress cracking.

5. Conclusions

Strain field measurements have been managed on outside surface of petaloid bases of PET bottles that are 3D surfaces. Validity of these measures has been verified with measures managed on well known solids of similar dimensions.

Finite element numerical simulations have been managed assuming the PET exhibits an isotropic elastic behaviour. The stress field, not influenced much by elastic properties, allows an evaluation of the elastic modulus by comparing the stresses evaluation to the measured strains.

The PET material of the petaloid bases is clearly heterogeneous and anisotropic when far from the injection point. Higher modulus are in the radial direction almost everywhere which shows that the macromolecules of the PET have been more stretched in the radial direction than in the circumferential one. Elongation of macromolecules is responsible for induced anisotropy.

The non linear effect of the LV base necessitates taking into account the entire bottle influence to reproduce similar evolution of stress and strain versus internal pressure. The modelling of the base only leads to too severe boundary conditions and stresses obtained by finite element simulation do not match with the strain measures.

The non linear behaviour of the LV base confirms the “come and go” bending effect during the internal pressure evolution for this bottle. It also explains the better resistance of this base to ESC test. On the other hand, the identification procedure of the Young modulus will be more complex because it must take into account the complete history of the base loading.

One must confirm the identification made by managing a new finite simulation where the orthotropic elasticity is implemented in Patran-Nastran to make sure that stresses and strain match. Another confirmation can be done experimentally by cutting specimens from the base to manage modulus measures.

Finally, these new data will help to the development of a viscoelastic law coupled with microstructural parameters as crystal ratio or macromolecular orientation in order to manage numerical simulations of the blow molding process and accelerate the validation of the designed shape. In Cosson, 2008, authors proposed a full package, limited to axi symmetric

problems, which is able to simulate the stretch blow molding process and the evolution of the material microstructure in order to predict the elastic behavior of the final bottle. The simulation gives accurate results and the predicted modulus in the regular region of the bottle, where the PET is strongly stretched in circumferential and longitudinal directions, but is limited to axi symmetric geometry of bottles. In the perspective of 3D simulations of the process, our identifications on petaloid bases will help to validate the predicted modulus.

Appendix: Principe of the stereo correlation, corrections

The stereo correlation technique is based on the determination of the apparent displacement between two digital images of the same object taken by two cameras. The digital image correlation software named Correli^{GD} (Chevalier et al., 2001) has been adapted to transform displacements U and V of a node of the grid into the depth z of a point M of the 3D object.

In order to compare the two captured images, the user defines by two clicks, the zone of interest (ZOI) in the reference image. The size of this zone is PxQ in pixel where P and Q are integers. To map the whole ZOI, the second parameter to choose is the shift δx (= δy = S) between two consecutive points where the displacement will be calculated. This generates a regular grid. The user specifies also the size of a mask (the region of interest around a point of the grid) by setting the value of M (< P and Q). These two parameters define the mesh formed by the centre of each mask used to analyze the displacement field (see Fig.16). The following analysis is performed for each mask independently. It follows that parallel computations can be used in the present case. A first FFT correlation is carried out and a first value of the in-plane displacement correction ΔU, ΔV is obtained. The values ΔU, ΔV are again integer numbers so that the mask in the deformed image can be displaced by an additional amount ΔU, ΔV. The displacement residual are now less than 1/2 pixel in each direction.

A cross-correlation is performed. A sub-pixel correction of the displacement δU, δV is obtained by determining the maximum of a parabolic interpolation of the correlation function.

The interpolation is performed by considering the maximum pixel and its eight nearest neighbors. Therefore, one obtains a sub-pixel value. By using the 'shifting' property of the Fourier transform, one can move the deformed mask by an amount δU, δV. Since an interpolation was used, one may induce some errors requiring to re-iterate by considering the new 'deformed' mask until a convergence criterion is reached. The criterion checks whether the maximum of the interpolated correlation function increases as the number of iterations increases. Otherwise, the iteration scheme is stopped. The procedure, CORRELI^{GD} (Hild et al., 1999), was first implemented in Matlab^{TM}. An extension to the determination of a 3D surface has been developed since.

The two cameras are placed in a horizontal plane (O, y, z), the direction x is the vertical one. Let δU, δV be the components of the apparent displacement between the two pictures made of the cameras. In a perfect experiment δU should be null and δV related to the depth by Eq. A1 for small values of δV in regard of a.

$$z = -\frac{d}{2a+\delta V}\delta V \approx -\frac{d}{2a}\delta V \qquad \text{(A1)}$$

a is the half distance between the two cameras and d the distance between the object and the cameras. The precise value of a is easy to measure but, since the camera focal may vary (use of a zoom for the object to fit full screen) the measure of d necessitates a calibration using a known object.

Despite the identification of d, the method induces two sources of error that must be corrected. Figure 17a shows that the first estimation of the apparent displacement δU is not represented by a horizontal plane corresponding to a null value. A little difference between the focal of the two cameras induces an apparent strain that may be represented by the following displacement fields:

$$\begin{aligned} \delta U &= \varepsilon x + U_{0F} \\ \delta V &= \varepsilon y + V_{0F} \end{aligned} \qquad \text{(A2)}$$

This defect induces a slope in the x direction of the plane representing δU. Another source of error is due to default of parallelism between the two cameras. This difference induces a rotation between the two pictures that can be represented by the following relations:

$$\begin{aligned} \delta U &= -\theta y + U_{0R} \\ \delta V &= \theta x + V_{0R} \end{aligned} \qquad \text{(A3)}$$

Using the least square method to fit the θ and ε to minimize δU, one is able to make corrections on the δV component before application of the transformation Eq.A1. Figure 17b shows the corrected components δU (which is quasi horizontal) and δV.

The method of auto correlation induces noise in the apparent displacement fields measured. Considering the further use of this field to calculated strains from discrete derivation, it appears that a smoothing operation is necessary. This operation is managed using the least square method to evaluation the best tangent plane in the neighborhood of the studied point. The amplitude of the neighborhood is fixed by the parameter T (integer) that defines the number of cells to take into account in both x and y directions around the point studied. More T is important, more the smoothing operation will be. It is worth noting that the T value impact is related to the shift factor of the grid: for the same T value the smoothing effect will be different if S is high or low. On Fig.17c, one can see the final result: the smooth cylindrical shape of the measured surface.

List of tables

List of figures

Figure 2: Probability density function for the “time before cracking” variable. The LV base resists much better than the SV one. In both case, the crack initiate in the circumferential direction, between a foot and the injection point.

Figure 3: Stereo correlation apparatus, two CCD cameras are used and the apparent displacements U and V lead to the determination of the depth z.

Figure 4: the cylinder and the bloc have been painted in black with random white spots. Two digital images taken from two different points of view allow the numerical construction of the 3D surface by stereo correlation.

Figure 5: Bottle bases construction in a circular zone around the injection point (PI) and visualization of the displacement field when bottles are under internal pressure. Left, SV base and right, LV base.

Figure 6: Petaloid base cut in a median plan, thickness distribution

Figure 7: Axis label and geometrical definition of the surface description

Figure 8: Results of the 3D strain field measurement: (a) definition of the region of interest; (b) and (c) distribution of the principal strains ε_1 and ε_2 and principal directions for SV, (d) and (e) the same for LV base.

Figure 9: Strain components evolution versus internal pressure at the injection point. ε_{xx} (circles) and ε_{yy} (stars) have the same evolution: the strain is purely biaxial. Strain evolution is quasi linear for SV from 0 to 5 bar but a clear non linearity can be seen for LV.

Figure 10: Linear shell elements used to mesh the petaloid base (about 24000 nodes). (a) boundary conditions applied on the top circle: $u_\theta = u_z = 0$; (b) implementation of the thickness evolution measured on the bottle base (Fig.8).

Figure 11: Finite element simulation on SV for an internal pressure of 5 bar. (a) the major principal stress σ_1 ; (b) the mid principal stress σ_2 on the 3D outside surface of the petaloid base ; (c) the principal direction associated to σ_1.

Figure 12: Principal stresses at the injection point for SV (a) and LV (b) bases. σ_1 and σ_2 are equal: the loading is purely biaxial. The evolution of stress versus internal pressure is linear for the SV base but LV base highlights a non linear effect.

Figure 13: Identification of Young's modulus for anisotropic materials, distributions of modulus E_1 and E_2 for the SV petaloid base.

Figure 14: LV and SV petaloid base after a heating stage at 120°C. The white zone delimitates the initially amorphous zone of the base.

Figure 15: Distribution of finite element principal stresses versus distance from the injection point (top) and principal strains obtained by stereo correlation measure (bottom).

Figure 16: Illustration of each parameter: zone of interest selected (solid rectangle), mask size (dashed square) and nodes of the regular grid (dot). The contour plot shows the isovalues of the component V of the displacement between the two images.

Figure 17: correction of defects of focal and parallelism between the two cameras: (a) raw apparent displacements δU and δV, (b) corrected apparent δU and δV (δU component is quasi horizontal and naught), (c) surface representation from corrected δV before and after the smooth operation.

References

Bruck, H.A., et al., ‘Digital image correlation using Newton–Raphson method of partial differential correction’, Exp Mech 29 (3), 261–267 (1989)

Cakmak, M., et al., ‘Structural characterization of crystallinity and crystalline orientation in simultaneously biaxially stretched and annealed polyethylene terephthalate films’, J. of Polymer Engineering, 37, 291-312 (1986)

Chang, H., et al., ‘Morphology of Biaxially Stretched Poly (ethylene terephthalate) Films’, J. Macromol. Sci.–Phys., B32 (1), 99-123 (1993)

Chevalier, L., et al., ‘Induced crystallinity during stretch-blow moulding process and its influence on mechanical strength of poly(ethylene terephthalate) bottles’, Plastics rubber and composites 28, 8, 393-401 (1999)

Chevalier, L., et al., ‘Digital image correlation used to analyze the multiaxial behavior of rubber-like materials’, European Journal of Mechanics - A/Solids, 20 (2), 169-187 (2001)

Chevalier, L., Marco, Y., ‘Tools for multiaxial validation of behavior laws chosen for modeling hyper-elasticity of rubber-like materials’, Pol. Eng. Sci., 42, 280-298 (2002)

Cosson, B., ‘Modélisation et simulation numérique du procédé de soufflage par bi-orientation des bouteilles en PET : évolution de microstructure, évolution de comportement’, PhD Thesis University Paris-Est (2008)

Garcia, D., et al., ‘A Combined Temporal Tracking and Stereo-correlation Technique for Accurate Measurement of 3D Displacements: Application to Sheet Metal Forming’, Journal of Materials Processing Technology, 125-126, 736-742 (2002)

Garcia, D., Orteu, J.J., ‘3D Deformation measurement using stereo-correlation applied to the forming of metal or elastomer sheets, in: Proceedings of the International Workshop on Video-controlled Materials Testing and In-situ Microstructural Characterization’, Nancy, France, November 16–18 (1999)

Hamid, R., ‘Distributed stereo-correlation algorithm’. Computer Communications, 19 (8), 707-711 (1996)

Hanley, T., et al., ‘Molecular morphology of petaloid bases of PET bottles: A small-angle X-ray scattering study’, J. Applied Polymer Science, 99 (6), 3328-3335 (2006)

Haudin, J.M., Monasse, B., ‘Introduction la mécanique des polymères’, INPL- MECAMAT-GFP-APOLLOR-FIRTECH, 97-115 (1996)

He, Z.H., et al., ‘Two-dimensional fluid velocity measurements by use of digital speckle correlation techniques’, Exp Mech 24 (2), 117–121 (1984)

Helm, J.D., et al., ‘Improved 3D image correlation for surface displacement measurement’, Opt. Eng., 35 (7), 1911–1920 (1996)

Hild, F., et al., ‘Mesure de champs de déplacement 2D par intercorrélation d’images : CORRELI2D’, internal report 230, LMT-Cachan (1999)

Lapersonne, P., et al., ‘Molecular orientation and conformational changes due to uniaxial-planar deformation of poly(ethylene terephthalate) films’, Polymer, 33, 1277-1283 (1992)

Le Bourvellec, G., et al., ‘Amorphous orientation and induced crystallization in uniaxially stretched poly(ethylene terephthalate glycol)’, Polymer, 27, 856-860 (1986)

Le Bourvellec, G., Beautemps, J., ‘Stretching of PET films under constant load. II. Structural analysis’, J. of App. Pol. Sci., 39, 329-339 (1990)

Luo, P.F., et al., ‘Application of stereo vision to 3D deformation analysis in fracture experiments’, Opt. Eng., 33 (3), 981–990 (1994)

Marco, Y., et al., ‘Induced crystallization and orientation of polyethylene terephthalate during uniaxial and biaxial elongation’, Macromolecular Symposia, 185, 15-34 (2002)

Marco, Y., ‘Caractérisation multi-axiale du comportement et de la micro-structure d'un semi-cristallin : application au cas du P.E.T.’, Ph D Thesis of ENS de Cachan (2003)

Mistou, S., et al., ‘Mesure 3D sans contact des déplacements et déformations sur des films plastiques transparents par stéréo-corrélation3D non-contact measurement of strain and displacement on transparent plastic films by stereo correlation’, Mécanique & Industries, 4 (6), 637-664 (2003)

Peters, W.H., Ranson, W.F., ‘Digital imaging techniques in experimental stress analysis’, Opt. Eng., 21 (3), 427–431 (1982)

Peters, W.H., et al., ‘Application of digital correlation methods to rigid body mechanics’, Opt. Eng., 22 (6), 738–742 (1983)

Picard, M., Billon, N., ‘Microstructural Evolution of PET under Stretching and during Stretch Blow Moulding’, 10th ESAFORM Conference on Material Forming, Zaragoza, SPAIN, 907, 801-806 (2007)

Pople, J.A., et al., ‘The Development of Organized Structures in Polyethylene Crystallized from a Sheared Melt, Analyzed by WAXS and TEM’, Polymer, 40, 2769-2777 (2000)

Réthoré, J., et al., ‘From pictures to extended finite elements: extended digital image correlation (X-DIC)’, Comptes Rendus Académie des Sciences : Mécanique, 335 (3), 131-137 (2007)

Réthoré, J., et al., ‘An extended and integrated digital image correlation technique applied to the analysis fractured samples’, Eur. J. Comput. Mech. 18, 285-306 (2009)

Reynolds, A.P., Duvall, F., ‘Digital image correlation for determination of weld and base metal constitutive behavior’, Welding J., 78 (10), 355s–360s (1999)

Roux, S., et al., ‘Three-dimensional image correlation from X-ray computed tomography of solid foam’, Composites Part A: Applied Science and Manufacturing, 39, (8), 1253-1265 (2008)

Salem, D.R., ‘Development of crystalline order during hot-drawing of poly(ethylene terephthalate) film: influence of strain rate’, Polymer, 33, 15, 3182-3188 (1992)

Salem, D.R., ‘Microstructure development during constant-force drawing of poly(ethylene terephthalate) film’, Polymer, 39 (26), 7067-7077 (1998)

Shen, D.Y., et al., ‘Conformational changes of amorphous poly(ethylene terephthalate) films during uniaxial stretching’, Macromolecular Chemistry and Physics, 192 (2), 301-307 (1991)

Spiby, S., et al., ‘An infra-red study of conformational changes occurring during the drawing of PEMT, PET and PEMT/PET copolymer’, Polymer, 33, 4479-4485 (1992)

Sutton, M.A., et al., ‘Determination of displacements using an improved digital correlation method’, Image Vision Comput., 1 (3), 133–139 (1983)

Sutton, M.A., et al., ‘Application of an optimized digital correlation method to planar deformation analysis’, Image Vision Comput., 4 (3), 143–15 (1986)

Titomanlio, G., et al., ‘On the simulation of thermoplastic injection moulding process’, Intern. Polym. Processing, 12, 45-53 (1997)

Vigny, M., et al., ‘Study of the molecular structure of PET films obtained by an inverse stretching process. Part I: Constant speed drawing of amorphous films’, J. Polymer Engineering and Science, 37 (11), 1785-1794 (1997)

Li X.Y., ‘Environmental Stress Cracking Resistance of a New Copolymer of Bisphenol-A’, Polymer Degradation and Stability, 90 (1), 44-52 (2005)

Yan, J., et al., ‘Characterization of heterogeneous response of pipeline steel weld using digital image correlation’, SEM annual conference and exposition on experimental and applied mechanics, St Louis, Missouri, USA, 1, 90–96 (2006).

Table

	LV	**SV**
Mean failure time	51.3	17.7 min
Sdt. variation	13.6	14.2 min
Minimum failure time	21.0	1.0 min
Maximum failure time	> 60.0	58.0 min

Table 1: comparison of the resistance to ESC test between SV or LV bottles

	e_∞	e_M	r_0	L
SV	0.30	3.10	8.80	12.23
LV	0.33	3.20	9.05	15.40
Units	mm	mm	mm	Mm

Table 2: Values of the identified parameters for the thickness interpolation function.

Figure

Figure 1: 2L soda bottle petaloid bases, small valley (SV) between feet (left) or large valley (LV) between feet (right)

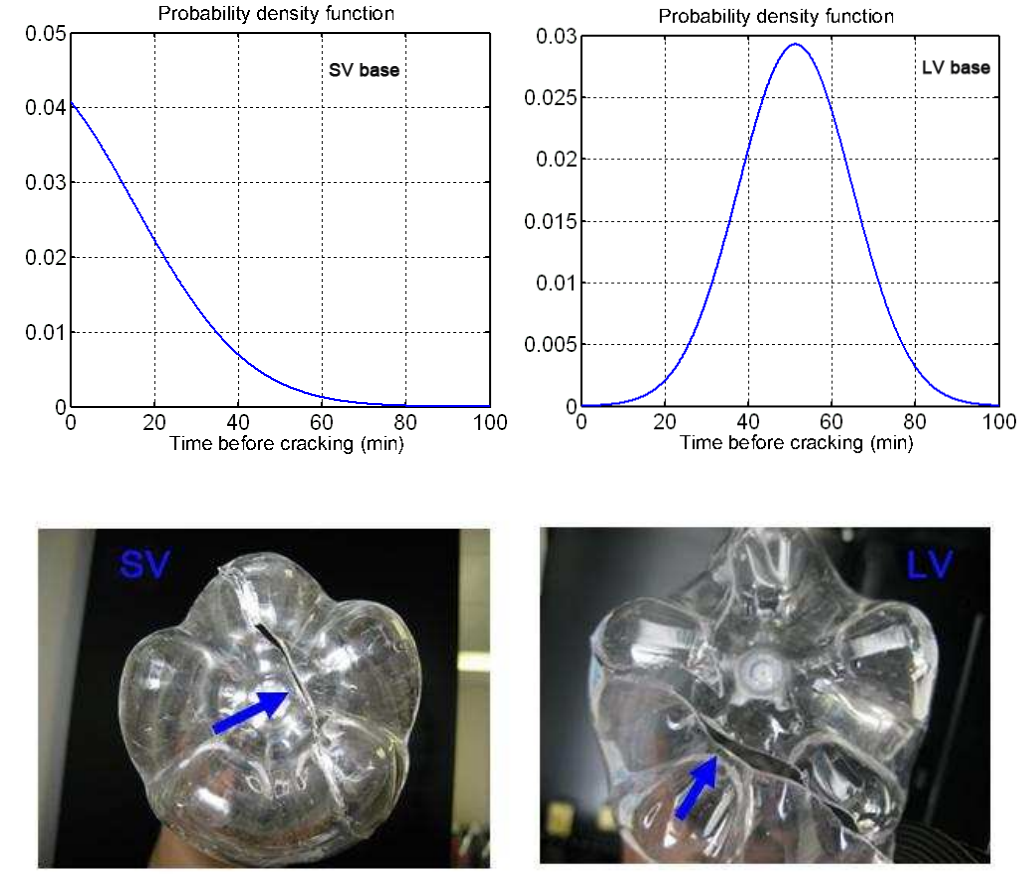

Figure 2: Probability density function for the "time before cracking" variable. The LV base resists much better than the SV one. In both case, the crack initiate in the circumferential direction, between a foot and the injection point.

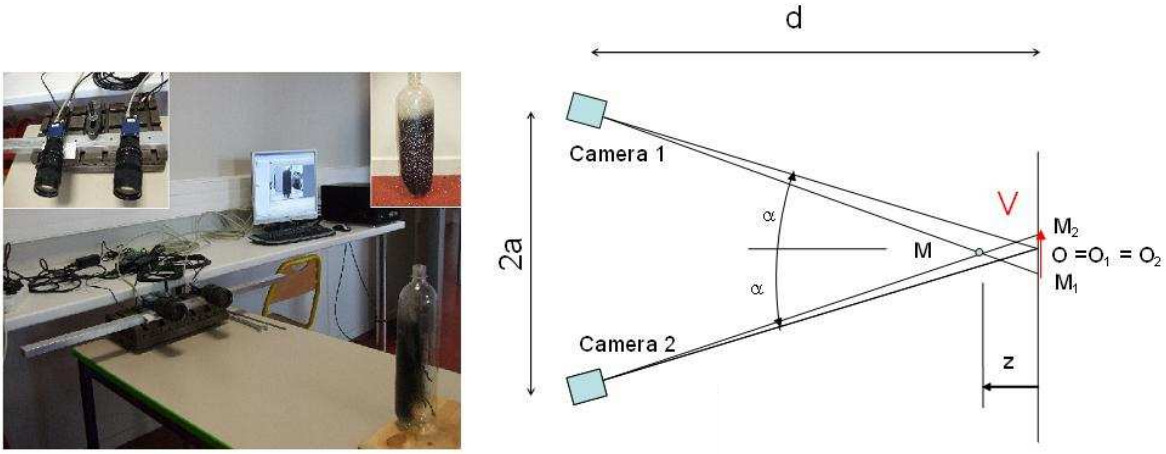

Figure 3: Stereo correlation apparatus, two CCD cameras are used and the apparent displacements U and V lead to the determination of the depth z.

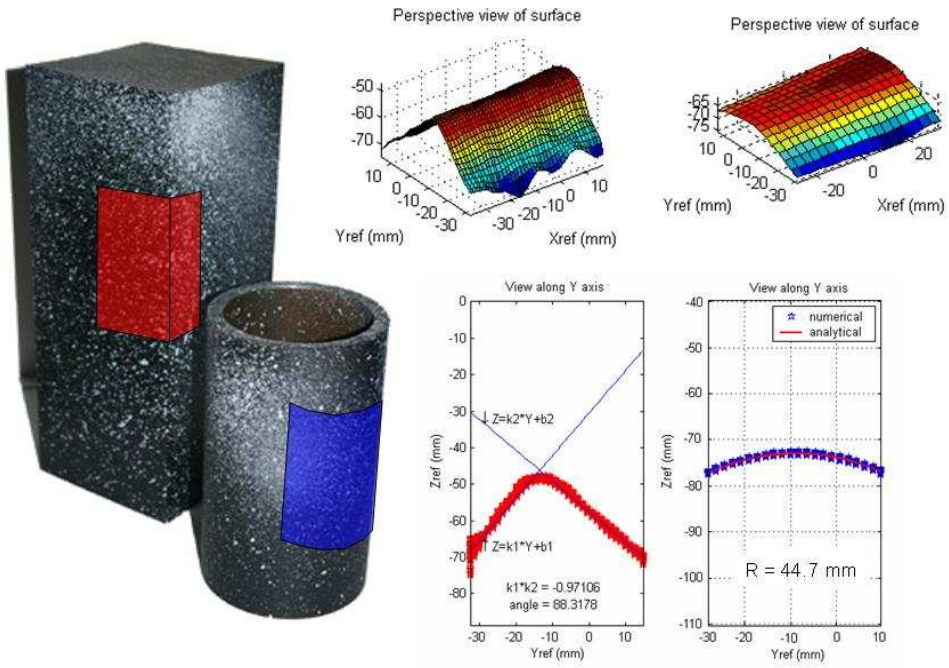

Figure 4: the cylinder and the bloc have been painted in black with random white spots. Two digital images taken from two different points of view allow the numerical construction of the 3D surface by stereo correlation.

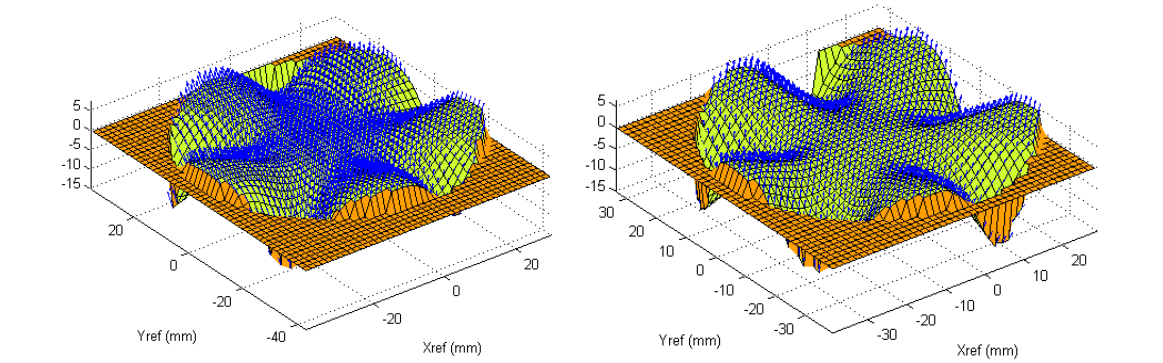

SV LV

Figure 5: Bottle bases construction in a circular zone around the injection point (PI) and visualization of the displacement field when bottles are under internal pressure. Left, SV base and right, LV base.

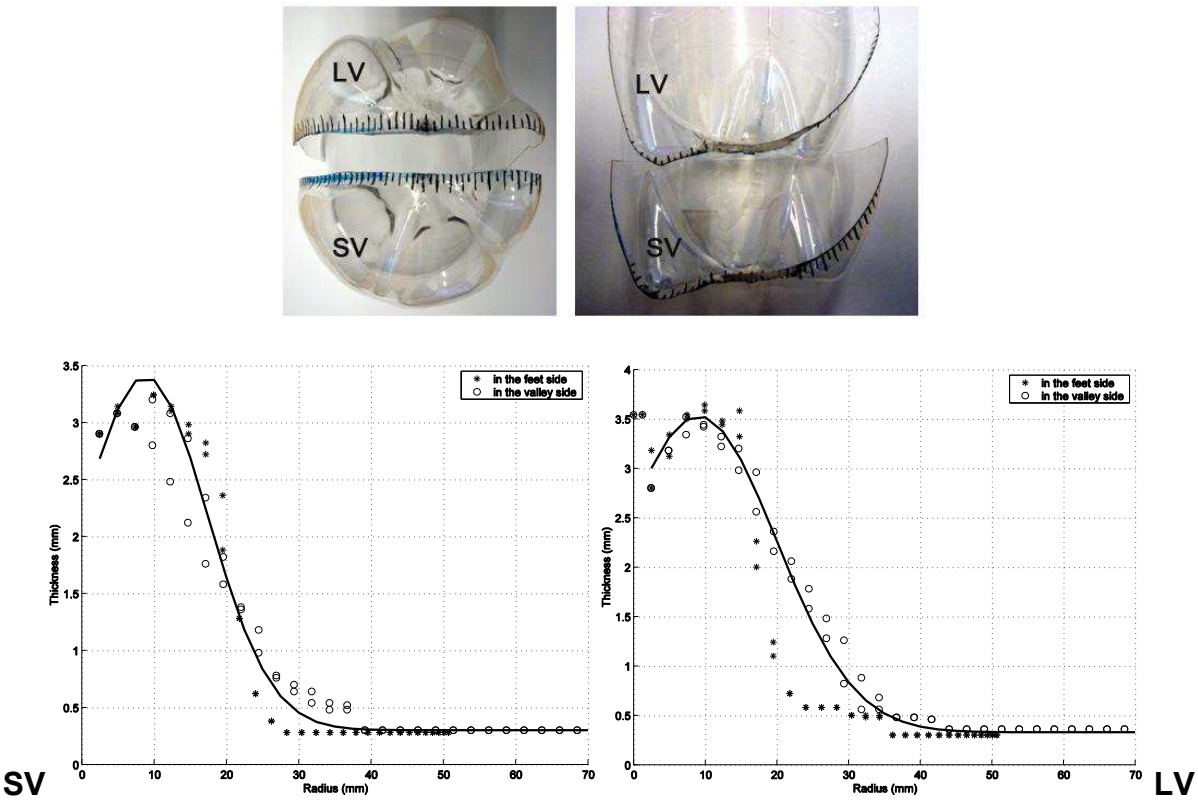

SV LV

Figure 6: Petaloid base cut in a median plan, thickness distribution

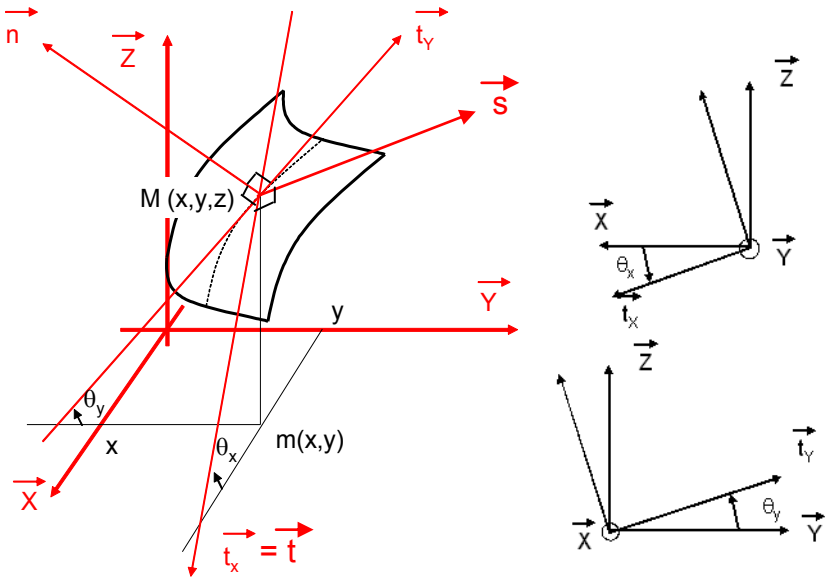

Figure 7: Axis label and geometrical definition of the surface description

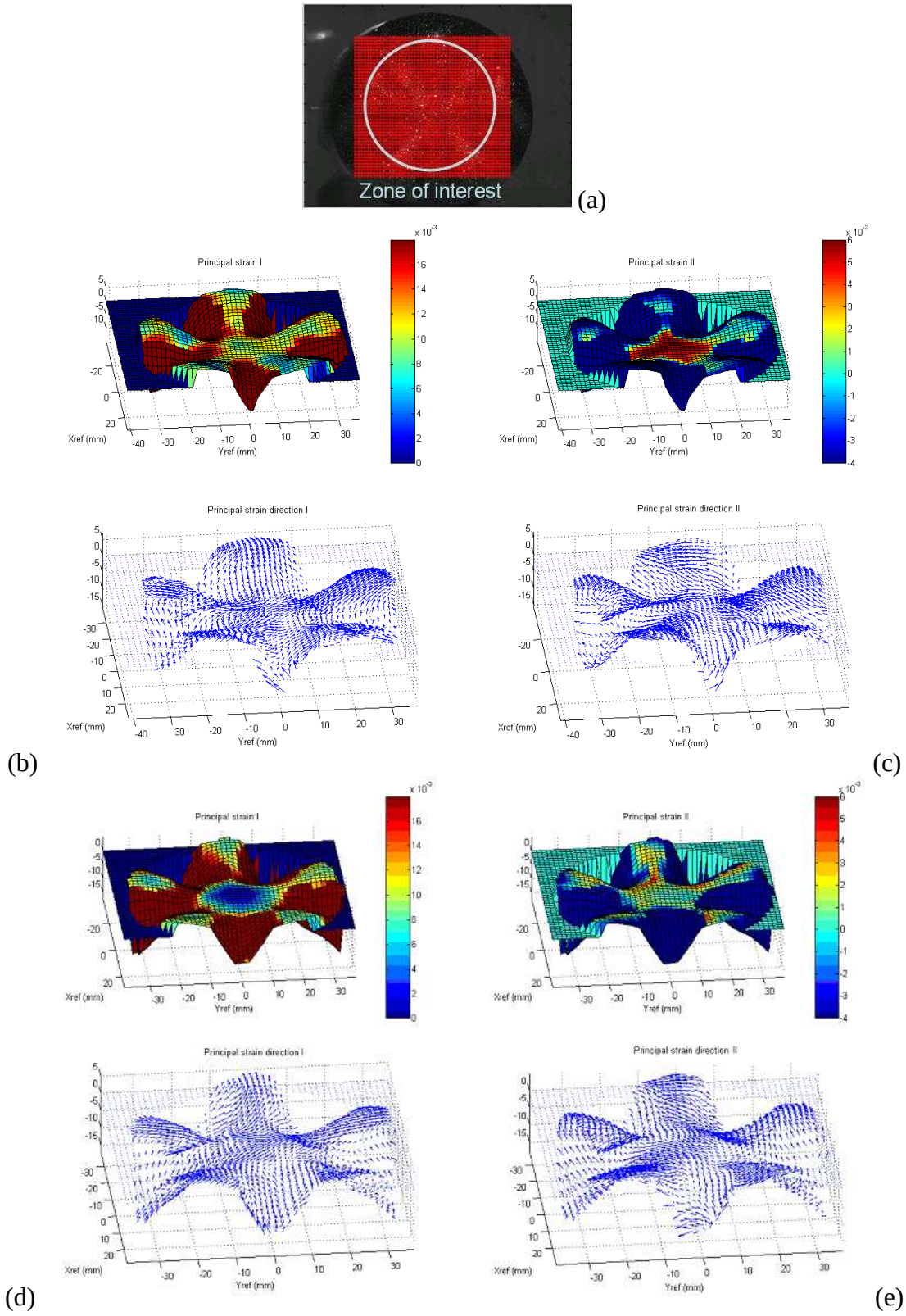

Figure 8: Results of the 3D strain field measurement: (a) definition of the region of interest; (b) and (c) distribution of the principal strains ε_1 and ε_2 and principal directions for SV, (d) and (e) the same for LV base.

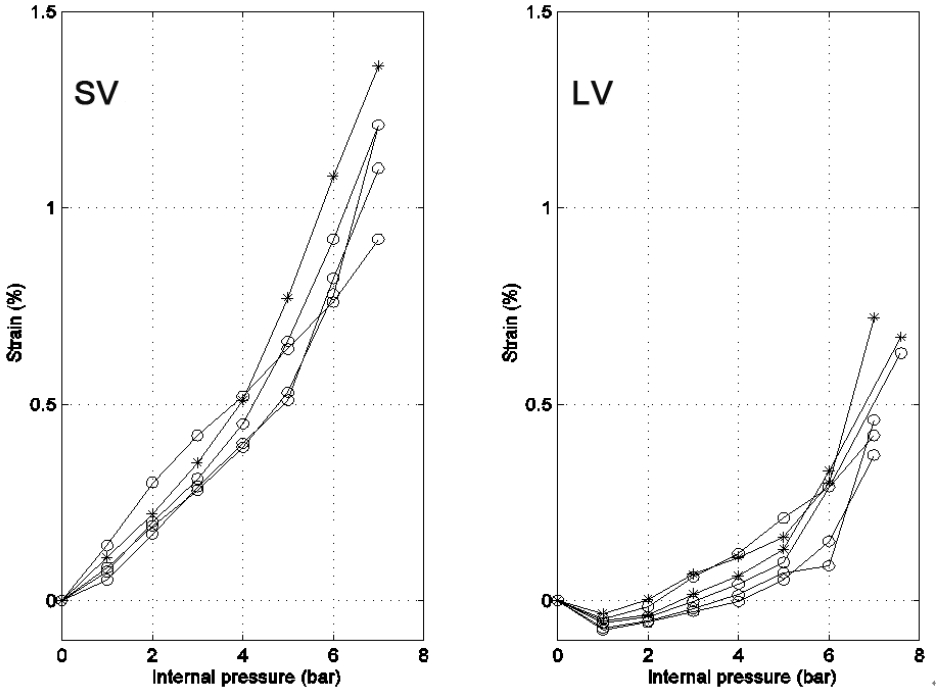

Figure 9: Strain components evolution versus internal pressure at the injection gate. ε_{xx} (circles) and ε_{yy} (stars) have the same evolution: the strain is purely biaxial. Strain evolution is quasi linear for SV from 0 to 5 bar but a clear non linearity can be seen for LV.

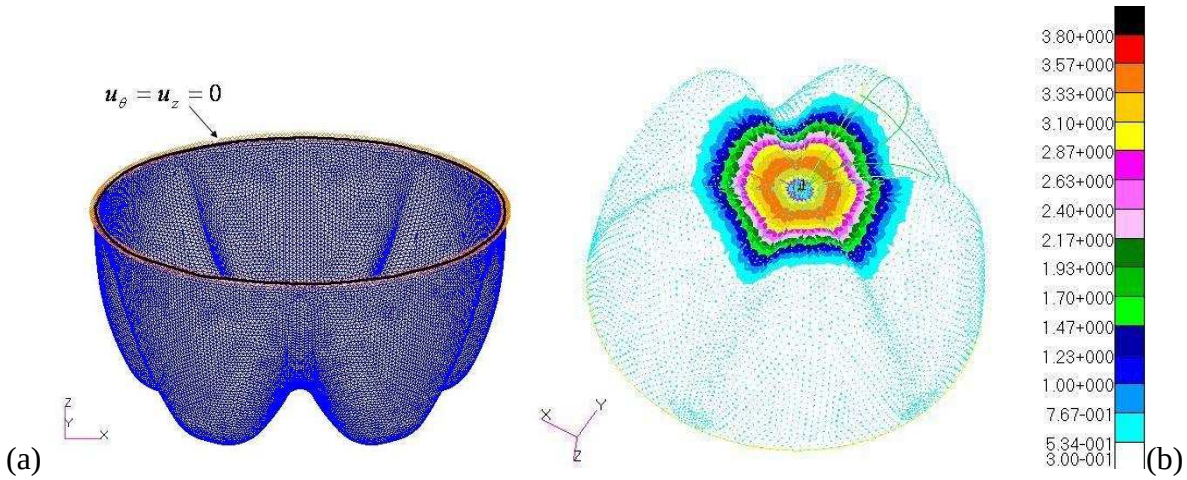

(a) (b)

Figure 10: Linear shell elements used to mesh the petaloid base (about 24000 nodes). (a) boundary conditions applied on the top circle: $u_\theta = u_z = 0$; (b) implementation of the thickness evolution measured on the bottle base (Fig.8).

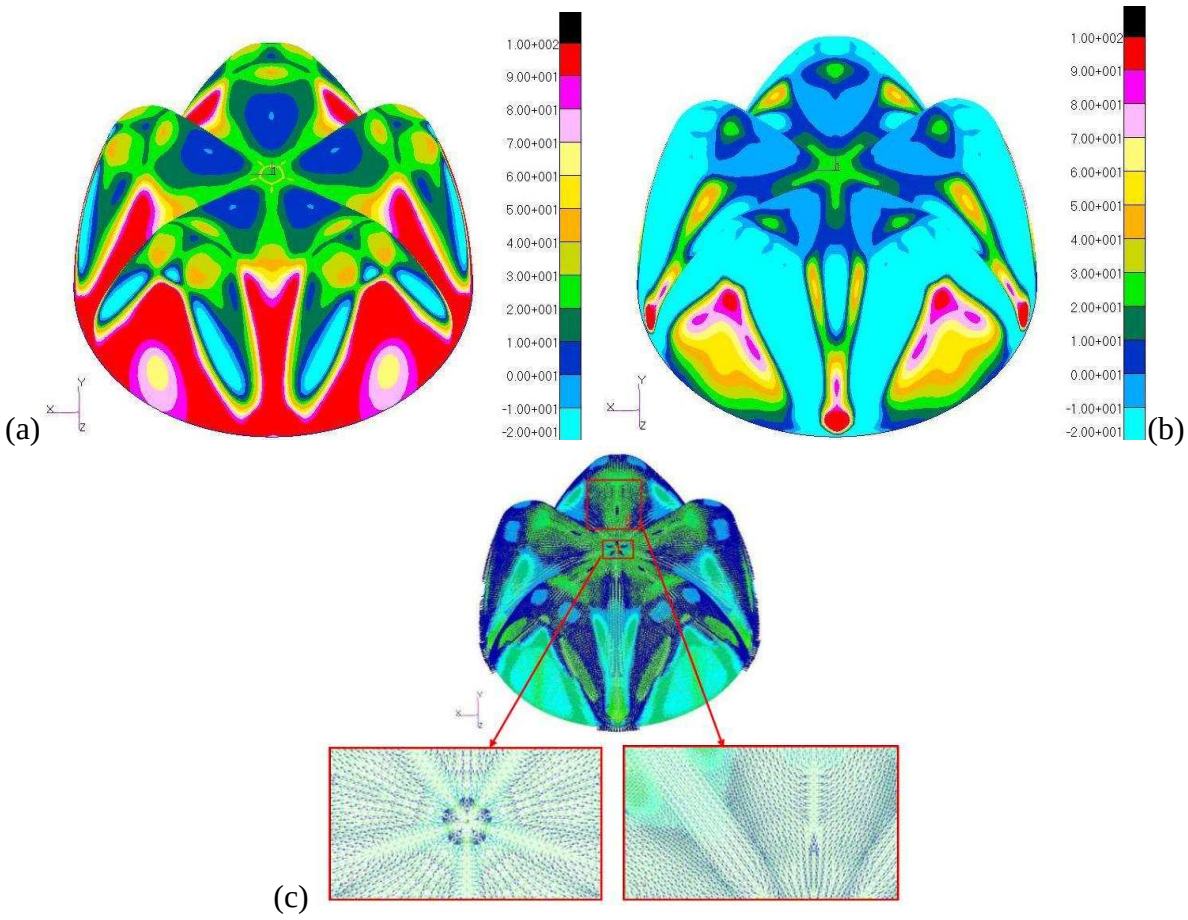

Figure 11: Finite element simulation on SV for an internal pressure of 5 bar. (a) the major principal stress σ_1 ; (b) the mid principal stress σ_2 on the 3D outside surface of the petaloid base ; (c) the principal direction associated to σ_1.

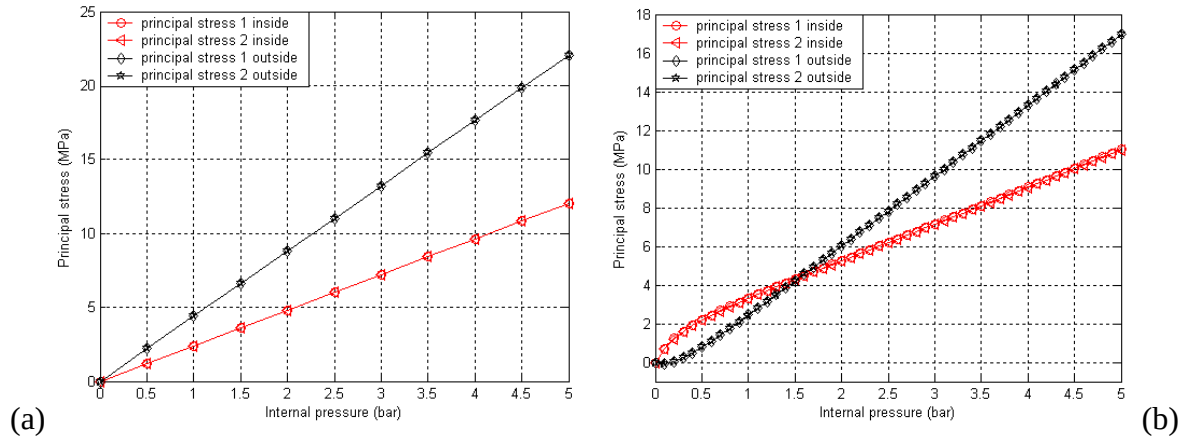

Figure 12: Principal stresses at the injection gate for SV (a) and LV (b) bases. σ_1 and σ_2 are equal: the loading is purely biaxial. The evolution of stress versus internal pressure is linear for the SV base but LV base highlights a non linear effect.

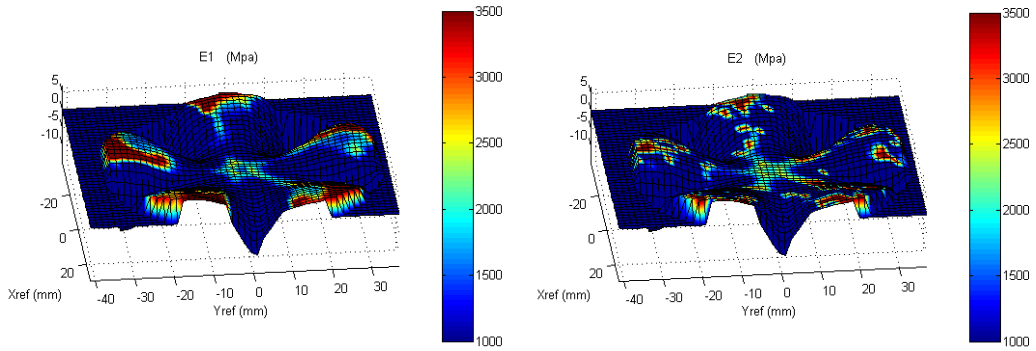

Figure 13: Identification of Young's modulus for anisotropic materials, distributions of modulus E_1 and E_2 for the SV petaloid base.

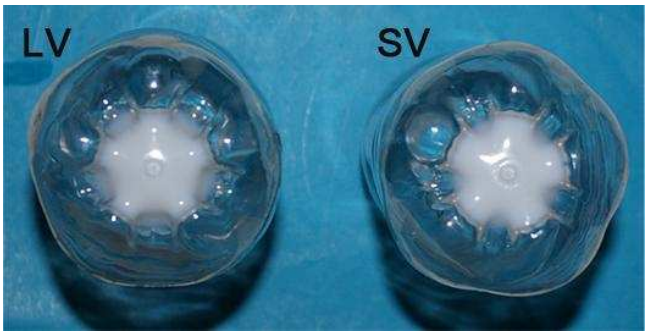

Figure 14: LV and SV petaloid base after a heating stage at 120°C. The white zone delimitates the initially amorphous zone of the base.

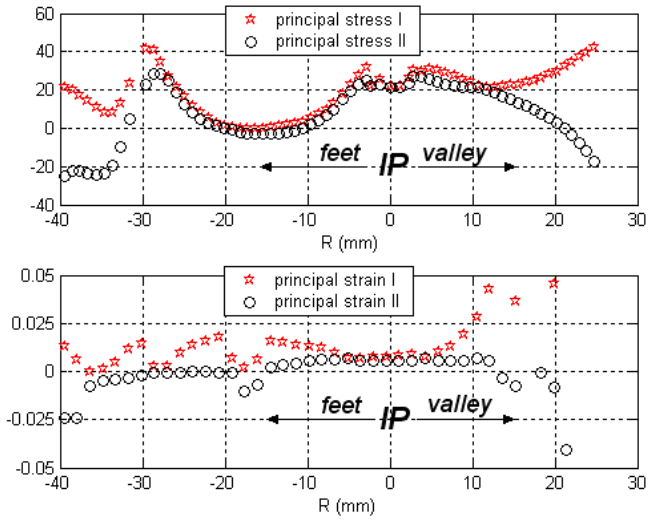

Figure 15: Distribution of finite element principal stresses versus distance from the injection gate (top) and principal strains obtained by stereo correlation measure (bottom).

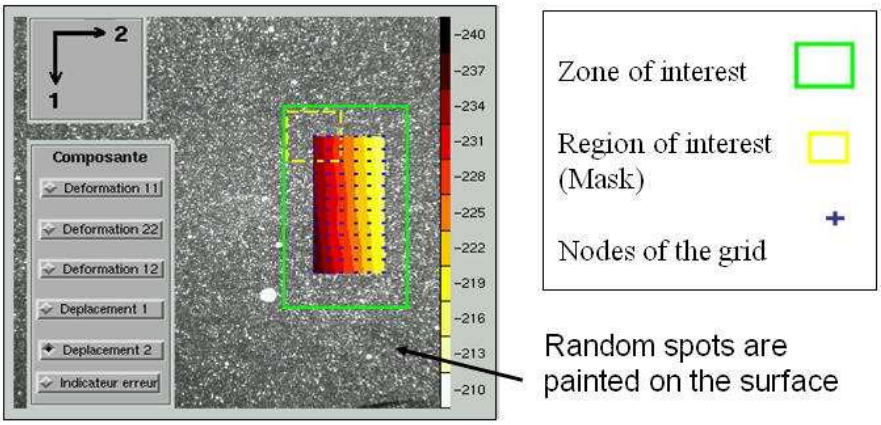

Figure 16: Illustration of each parameter: zone of interest selected (solid rectangle), mask size (dashed square) and nodes of the regular grid (dot). The contour plot shows the isovalues of the component V of the displacement between the two images.

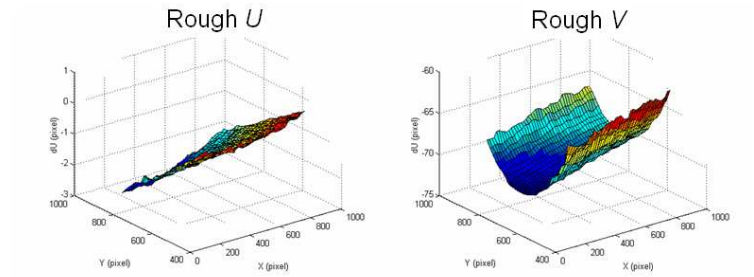

(a)

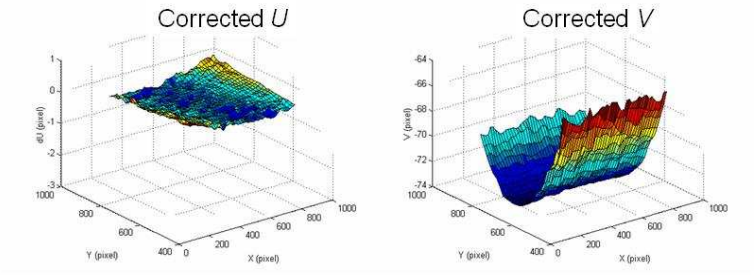

(b)

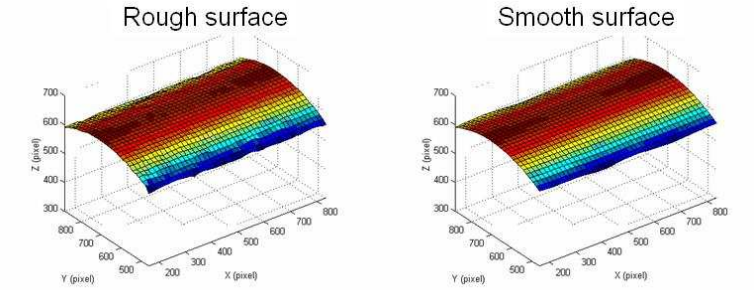

(c)

Figure 17: correction of defects of focal and parallelism between the two cameras: (a) raw apparent displacements δU and δV, (b) corrected apparent δU and δV (δU component is quasi horizontal and naught), (c) surface representation from corrected δV before and after the smooth operation.